# Supporting Information

# Potential-Driven In Situ Formation of CuS@$Cu_2Se$ with Se-Vacancy-Rich for Steering the $CO_2$ Electroreduction Path from HCOOH to $C_2H_5OH$

Shuxian Xie[a]‡, Chao Lv[a]‡, Lichun Kong[a], Cui Li[a], Chang Wang[a], Xuyu Lv[a], Qianmin Wu[a], Jiuju Feng[a], Ai-Jun Wang[a]*, De-Li Chen[a]*, Fa Yang[a]*

[a] Key Laboratory of the Ministry of Education for Advanced Catalysis Materials, College of Chemistry and Materials Science, Zhejiang Normal University, Jinhua, Zhejiang 321004, China.

‡These authors contribute equally to this work.

*E-mail: yangfa@zjnu.edu.cn; chendl@zjnu.cn; ajwang@zjnu.cn

## Experimental Section

**Chemicals.** Copper sulfate pentahydrate ($CuSO_4 \cdot 5H_2O$, GR) and Se powder (≥99.99%) were purchased from Aladdin. L-Ascorbic acid ($C_6H_8O_6$, ≥99.0%) were purchased from Macklin. Sodium citrate(anhydrous，≥98.0%) were purchased from Sigma-aldrich. Sodium hydroxide (NaOH, AR), Sodium sulfide ($Na_2S \cdot xH_2O$, 44.0%), Sodium borohydride ($NaBH_4$, AR), Hydrochloric acid (HCl, AR) and Potassium sulfate ($K_2SO_4$, AR) were purchased from Sinopharm Chemical Reagent Co. Ltd. Dimethyl sulfoxide (DMSO, 99.99%), $D_2O$ (99.99% deuterium atom) and Nafion solution (5 wt%) were purchased from Sigma-Aldrich. All reagents were of analytical grade and used without further purification. Deionized water (18.2 MΩ·cm) was used in all solution preparations. Nitrogen ($N_2$, 99.999%), Argon (Ar, 99.999%) and Carbon dioxide ($CO_2$, 99.999%) were purchased from Datong Co., Ltd.

**Instrumentation.** Transmission electron microscopy (TEM) and high resolution TEM (HRTEM) were performed using a JEOL JEM-2100 electron microscope with an operating voltage of 200 kV. X-ray photoelectron spectra (XPS) were collected on an ESCALab 250 X-ray photoelectron spectrometer with Al-Kα radiation. The binding energies obtained in the XPS spectral analysis were corrected for specimen charging by referencing C1s to 284.6 eV. X-ray diffraction (XRD) measurements were performed using a Philips X'Pert Pro Super X-ray diffractometer with Cu-Kα radiation (λ =1.5418 Å). $^1$H-NMR was performed on a BRUKER AVANCE-Ⅲ 500 HD (Switzerland). Electron paramagnetic resonance (EPR) spectra were obtained by a Bruker EPR EMXplus-9.5/12 spectrometer to detect the presence and behavior of native defects. Electrochemical experiments were performed using a CHI 750E electrochemical work station (CH Instruments, Chenhua Co.).

### Catalysts synthesis and Electrodes preparation.

**Synthesis of $Cu_2O$ microspheres:** Firstly, copper sulfate pentahydrate (8.5 mmol) and sodium citrate (3.5 mmol) were added into 400 mL deionized water to form homogeneous solution. Then, 100 mL of NaOH (0.13 mol) solution was mixed with the above solution under continuous stirring. Next, 250 mL of L-ascorbic acid (0.03 M) solution was slowly poured in and the mixture was stirred at room temperature for 1 h. Subsequently, the precipitate was separated by centrifugation, washed three times with ethanol and water, and then vacuum dried overnight at 60 °C to obtain the yellow $Cu_2O$ powder.

**Synthesis of $Cu_2O$@CuS microspheres:** Dispersing 0.2 g of the prepared $Cu_2O$ microspheres into 200 mL $Na_2S$ (3 mmol) solution. After stirring at room temperature for 90 min, centrifugation, washing, and drying were performed to obtain the dark-green $Cu_2O$@CuS powder, which was collected for next use.

**Synthesis of hollow CuS@CuSe heteromicrospheres:** As described below, 0.3 g Se powder in 10 mL deionized water was adopted as the selenium source. 0.4 g $NaBH_4$ was added into above solution under vigorous stirring, defined as solution A. A solution of 0.2 g $Cu_2O$@CuS dispersed in 50 mL water was defined as solution B. Then, solution B dropwise injected into solution A and maintained stirred for another 15 min to form black precipitation. Subsequently, it was processed by centrifugation and washing, and dried under vacuum at 60 °C overnight to obtain the $Cu_2O$@CuS@CuSe black powder. Finally, in order to remove the $Cu_2O$ component, the collected $Cu_2O$@CuS@CuSe powder was immersed in a 0.35 M HCl solution and stirred at 80 °C for 4 h to obtain the desired CuS@CuSe catalyst. For comparison, the CuS microspheres were obtained by directly etching the above prepared $Cu_2O$@CuS microspheres. Meanwhile, a selenylation treatment and further etching process for $Cu_2O$ microspheres were performed to give hollow CuSe microspheres assembled with nanosheets.

**Electrocatalytic $CO_2$ reduction ($CO_2$RR).** Electrochemical $CO_2$RR measurements were performed in a customized gastight H-type glass cell separated by a cation-exchange membrane (CEM, Nafion 117). Electrode potentials were converted to the reversible hydrogen electrode (RHE) reference scale using $E_{RHE} = E_{Ag/AgCl} + 0.197 + 0.0591\times pH$. Each compartment holds 50 mL of electrolyte. The electrolyte was 0.5 M $K_2SO_4$ aqueous solution saturated with $CO_2$. Before the experiments, the electrolyte in the cathodic compartment was saturated with $CO_2$ by bubbling $CO_2$ gas for at least 30 min. During the reduction experiments, $CO_2$ gas was delivered at an average rate of 25 mL $min^{-1}$ (at room temperature and ambient pressure) and routed directly into the gas sampling loop of a gas chromatograph (Shimadzu-2014). The gas chromatograph was equipped with a thermal conductivity detector (TCD) for $H_2$ concentration quantification and a flame ionization detector (FID) coupled with a methanizer for quantifying CO concentration. Argon was used as the carrier gas and constituents of the gaseous sample were separated using two Porapak N80/100 columns packed with molecular sieve-13X. The GC was calibrated using different concentrations of calibration standards commercially available from YJ Technical Company.

The Faradaic Efficiency (FE) of gaseous products were calculated as below:

$$FE_s = \frac{zFv_sGP_0}{RT_0 i_{total}} \times 100\%$$

$$FE_s = \frac{\mathrm{z} \times 96485\left(\frac{C}{mol}\right) \times v_s(vol\%) \times G\left(\frac{mL}{min}\right) \times 10^{-6}\left(\frac{m^3}{mL}\right) \times 1.01 \times 10^5\left(\frac{N}{m^2}\right)}{8.314\left(\frac{N\,m}{mol\,K}\right) \times 298.15(K) \times i_{total}\left(\frac{C}{s}\right) \times 60\left(\frac{s}{min}\right)} \times 100\%$$

where $v_s$ (vol%) = volume concentration of s = gaseous products in the exhaust gas from the electrochemical cell (GC data), $P_0$ = 1.013 bar and $T_0$ = 298.15 K, gas flow rate (G) measured by a FL-1802 rotor meter at the exit of the electrochemical cell (mL $min^{-1}$), z is the number of electrons transferred for production formation, $i_{total}$ (mA) = steady-state cell current, F = 96485 C·$mol^{-1}$, R = 8.314 J·$mol^{-1}$·$K^{-1}$.

The total amount of liquid products were measured using NMR (AV 500) spectroscopy, in which 50 mL catholyte was first mixed with 5 μL dimethyl sulfoxide (internal standard, DMSO, Sigma, 99.99%), and then 0.5 mL of the mixture was taken out and mixed evenly with 0.1 mL of $D_2O$ (deuterated water) as the NMR samples. The Faradaic efficiency can be calculated as follows: $FE_{\text{liquid products}} = zF \times n_{\text{liquid products}} / (i_{total}\times t)$, where F is the Faraday constant, z is the number of electrons transferred for production formation, and *t* is the electrolysis time. The partial current densities of

$CO_2RR$ products were calculated as below, where electrode area is "$cm^2$". The unit of $j_{products}$ in the equations is "$mA/cm^2$".

$$j_{products} = FE_{products} \times i_{total} \times (electrode\ area)^{-1}$$

**Morphology and lattice analysis before and after electrolysis.** Firstly, 10 μL catalyst ink was dropped on Au-grid-supported carbon film and dried at room temperature during vacuum environment. Then TEM images were taken around some special marks so that we can find these areas exactly after the $CO_2RR$ experiments. After that, the Au-grid-supported carbon film was kept in a three-electrode sealed micro channel with outlet and inlet, and $CO_2$-saturated 0.5 M $K_2SO_4$ was injected into the cell as shown in Fig. 3a. Finally, the Au-grid was washed gently with small amount of water and TEM images were taken on the same locations based on the special marks found before on the sample grid.

**In situ Raman spectra tests.** The in situ laser confocal Raman (LabRAM, Horiba-JY) measurements were conducted in a three-electrode spectroelectrochemical cell filled with $CO_2$-saturated 0.5 M $K_2SO_4$ solution as shown in Fig. S18, using the CuS@CuSe materials loaded on glass carbon electrode as the working electrode, a Pt wire as the counter electrode, and Ag/AgCl (3 M KCl) as the reference electrode. During the $CO_2RR$, the $CO_2$-saturated electrolyte was continuously fed into the electrolytic cell at a rate of 30 mL $min^{-1}$ by using a high-performance liquid chromatography pump to replenish $CO_2$ and remove the generated hydrogen bubbles to avoid the interfere with Raman signal. Meanwhile, the in situ Raman tests were applied to probe the reaction process. The Raman shift was calibrated to 520 $cm^{-1}$ using a Si wafer. Raman spectra were collected in the range of 50 to 1000 $cm^{-1}$ using a 532 nm laser.

**In Situ ATR-SEIRAS Measurements.** The Au film working electrode on a reflecting plane of a Si prism was prepared according to the so-called "two-step wet process" initially developed by this group.[1] The Si prism with the Au film on was assembled into a spectro-electrochemical cell that was then fixed in an optics system (SPEC-I, Shanghai Yuanfang Tech.) built in the chamber of a Nicolet iS50 infrared spectrometer with a liquid nitrogen cooled MCT detector for electrochemical ATR-SEIRAS measurements at an incidence angle of ca. 60°. All ATR-SEIRAS spectra were given in absorbance units defined as $-\log(I/I_0)$, where I and $I_0$ represent the sample and reference spectra, respectively. After that, the spectra at different potentials and time were obtained based on $I_0$. Unless otherwise stated, the acquisition time for each single-beam spectrum in a real-time measurement is 5 s (approximately twenty two interferograms) at a spectral resolution of 4 $cm^{-1}$. A CHI 750E electrochemistry workstation (CH Instruments, Inc.) was used to measure the open circuit potential (OCP) and to control the electrode potential. A Pt mesh and an Ag/AgCl electrode (3 M KCl) were used as the counter and reference electrodes, respectively. A typical reactor of ATR-SEIRAS consisting of two chambers with three electrodes is shown in Fig. S27. Electrolytes were prepared by dissolving high-purity 0.5 M $K_2SO_4$ in Milli-Q water (18.2 MΩ·cm), and deaerated with high-purity Ar or $CO_2$ prior to each electrochemical or spectroelectrochemical measurement.

**In Situ DEMS measurement.** Online DEMS measurements were run on a PM-DEMS mass spectrometer equipped with a secondary electron multiplier detector (Shanghai Pro-tech Limited Company). Prior to data acquisition, DEMS background signals were pre-stabilized for 1 h and subtracted from m/z signals for quantitative analysis. The flow cell was used during the DEMS measurements. The setup of the DEMS flow cell is illustrated in Fig. S46. Carbon paper electrodes coated with CuS and CuSe electrocatalysts, Ag/AgCl, and carbon rods were used as the working electrode, the reference electrode and the counter electrode, respectively. LSV technology was employed from −0.5 to −1.1 V (vs. Ag/AgCl) at a scan rate of 5 mV $s^{-1}$ until the baseline kept steady. Then, the corresponding mass signals appeared. After the electrochemical test was over and the mass signal returned to baseline, the next cycle was started using the same test conditions to avoid accidental errors during DEMS measurements. After four cycles, the experiment ended.

**Computational methods:**

Density functional theory based calculations were performed in this study to investigate the stable structures of the CuSe, $Cu_2Se$ and $Cu_2Se$-$V_{Se}$ systems, and the reaction pathways for the $CO_2$ Hydrogenation. The Perdew-Burke-Ernzerhof (PBE) functional within the generalized gradient approximation was adopted to calculate the exchange and correlation interactions between electrons using the Vienna Ab initio simulation package (VASP) with version of 5.4.4.[2-4] To account for the dispersion interaction between the adsorbate and the surface, the Grimme's scheme DFT-D3 was used.[5] A planewave basis set with a kinetic cutoff energy of 500 eV and projector augmented wave (PAW) method were employed in this study.[6, 7] The five-layer $Cu_2Se$ (220) surface was modeled by a p (2×1) supercell with 40 Cu atoms and 20 Se atoms, the five-layer $Cu_2Se$-$V_{Se}$ (220) surface with 40 Cu atoms and 19 Se atoms, and the three-layer CuSe (110) surface was modeled by a p (1×1) supercell with 36 Cu atoms and 36 Se atoms as shown in Fig. 4g. For $Cu_2Se$ (220), the bottom three-layer atoms were fixed in the slab while the top two-layer atoms with adsorbates were relaxed during optimization. And the bottom two-layer atoms were fixed in the slab while the top one-layer atoms with adsorbates were relaxed one CuSe (110) during optimization. A 2×2×1 Monkhorst-Pack k-point mesh was utilized for the slab model.[8] The vacuum region was more than 20 Å in distance to avoid interactions between neighboring images under periodic boundary conditions.The convergence tolerance for energy and force was set at $10^{-5}$ eV and $10^{-2}$ eV·$Å^{-1}$, respectively. A Hubbard correction of U= 5.0 eV was applied to the d-orbitals of Cu in $Cu_2Se$ and CuSe for better correspondence to the experimental adsorption energetics.[9] The above mentioned parameters were tested to have a reliable results for the systems.

The adsorption energy in this work was defined as:

$$E_{\mathrm{ad}} = E(\mathrm{ad/surf}) - E(\mathrm{ad}) - E(\mathrm{surf})$$

where $E$(ad/surf), $E$(ad) and $E$(surf) are the total energies of the adsorbate binding to surface, free adsorbate in vacuum and clean surface, respectively. The chemical potential of H is calculated using the formula $\mu$(H) =1/2$\mu$($H_2$). The chemical potential of CHO/COH is calculated using the formula $\mu$(CHO/COH) = $\mu$(CO) + 0.5 $\mu$(H2), where $\mu$(CO) is the chemical potential of CO. The chemical potentials of $H_2$ and $H_2O$ are calculated in the vapor phase using the ideal gas approximation.[10]

The Gibbs free energies at 300 K and 1 atm are obtained from[11]

$$G(\mathrm{T}) = E + H(\mathrm{T}) - TS(\mathrm{T})$$

where E was the energy that could be directly obtained from the DFT calculations, and H(T) and TS(T) are enthalpy and entropy at a given temperature.

The free energy diagrams of $CO_2$RR were calculated on $Cu_2Se$ (220) and $Cu_2Se$-$V_{Se}$ (220) surfaces by considering the following sequential steps.[12]

$* + CO_2 (g) \rightarrow *CO_2$

$*CO_2 + H^+ + e^- \rightarrow *COOH$

$*COOH + H^+ + e^- \rightarrow *CO + H_2O$ (l)

$*CO + CO (g) \rightarrow 2*CO$

$2*CO + H^+ + e^- \rightarrow *OCCHO$

or $*CO + H^+ + e^- \rightarrow *CHO$

$*CO + H^+ + e^- \rightarrow *COH$

$*CO \rightarrow CO (g) + *$

The free energy diagrams of $CO_2$RR were calculated on CuSe (110) surface by considering the following sequential steps.

CO pathway:

$* + CO_2 (g) \rightarrow *CO_2$

$*CO_2 + H^+ + e^- \rightarrow *COOH$

$*COOH + H^+ + e^- \rightarrow *CO + H_2O$ (l)

$*CO \rightarrow CO (g) + *$

HCOOH pathway:

$* + CO_2 (g) \rightarrow *CO_2$

$*CO_2 + H^+ + e^- \rightarrow *OCHO$

$*OCHO + H^+ + e^- \rightarrow *HCOOH$

We also calculated the onset potential for the $Cu^0$ species formation by simulating surface Se was reduced to $H_2Se$ into the electrolyte, leading to the formation of metallic $Cu^0$ species on catalyst surface. The onset potential of $Cu^0$ species formation was calculated with the equation:[13]

$$\Delta \mathrm{G} = \mathrm{E(H_2Se)} + \mathrm{E(surface\text{-}}V_{\mathrm{Se}}) - 2\mathrm{E(H^+ + e^-)} - \mathrm{E(surface)} + \Delta\mathrm{ZPE} - \mathrm{T}\Delta + 2\mathrm{U}$$

where E(surface-$V_{Se}$) is the $Cu_2Se$-$V_{Se}$ (220) surface with another Se being removed, and this Se is near the first $V_{Se}$. When ΔG equals zero, U is the onset potential of $Cu^0$ species formation.

Hydrogenation of Se to $H_2Se$ on $Cu_2Se$-$V_{Se}$ (220), according to the following reaction steps.

$*(Se) + H^+ + e^- \rightarrow H*(Se)$

$H*(Se) + H^+ + e^- \rightarrow 2H*(Se)$

$2H*(Se) \rightarrow H_2Se + *(V_{Se})$

For the proton-coupled electron transfer reaction steps, the computational hydrogen electrode (CHE) method was employed and the free energy corrections for the gas-phase species are calculated by VASPKIT 1.4.0.[14] All visualization of structure models are plotted using Visualization for Electronic and Structural Analysis (VESTA).[15]

## Supporting Figures and Tables

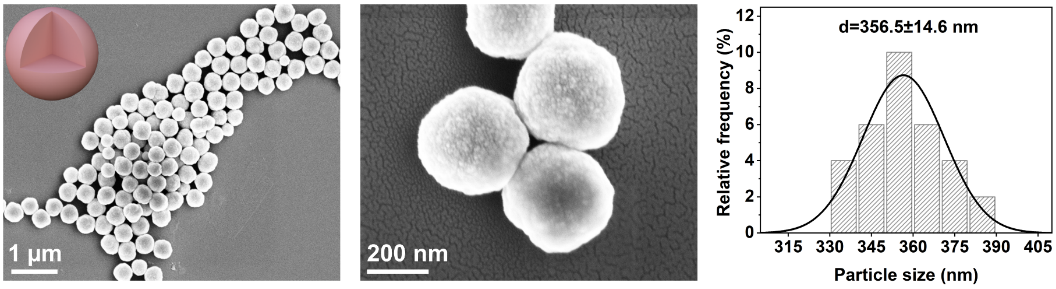

**Fig. S1.** Typical SEM images and corresponding size distributions of the $Cu_2O$ precursor.

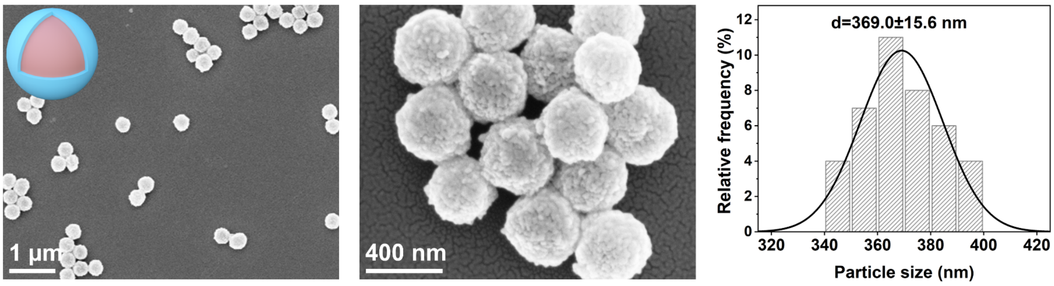

**Fig. S2.** Typical SEM images and corresponding size distributions of the $Cu_2O$@CuS precursor.

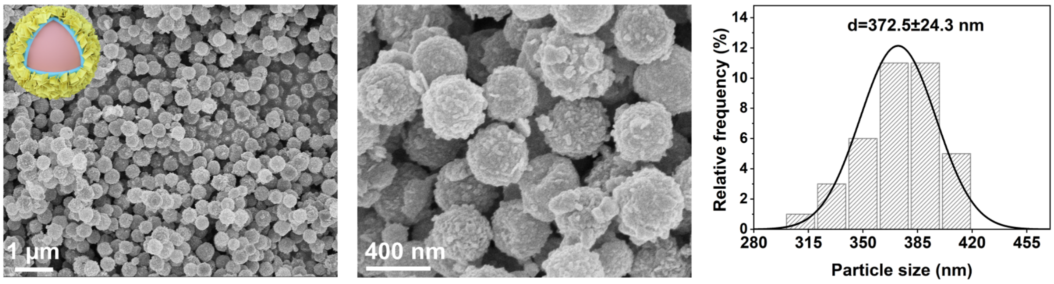

**Fig. S3.** Typical SEM images and corresponding size distributions of the $Cu_2O$@CuS@CuSe precursor.

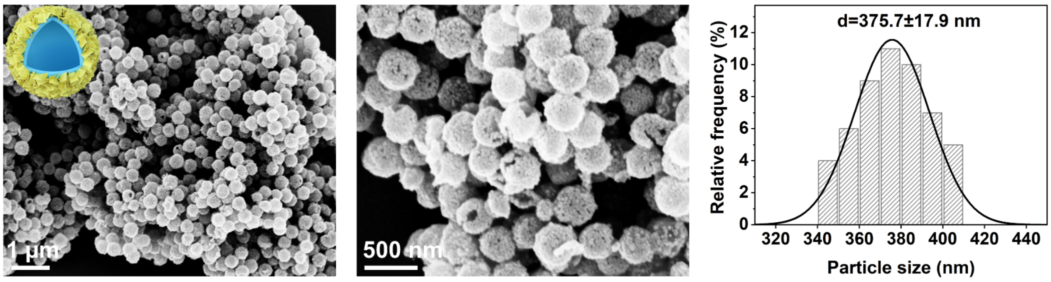

**Fig. S4.** Typical SEM images and corresponding size distributions of the CuS@CuSe sample.

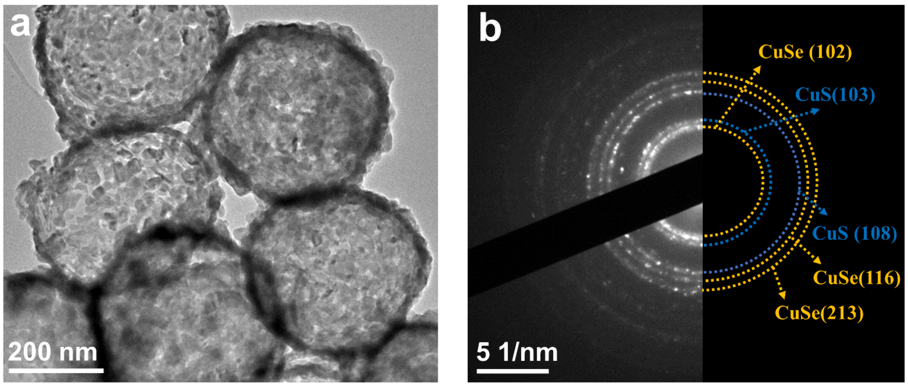

**Fig. S5.** (a) TEM image and (b) SAED pattern of the CuS@CuSe.

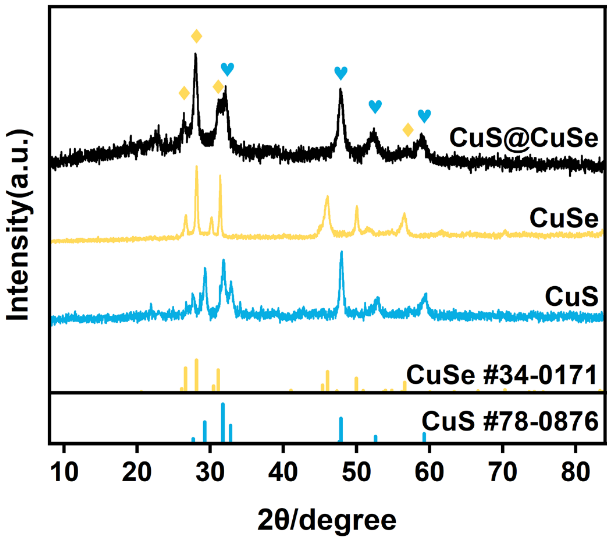

**Fig. S6.** XRD patterns of the CuS@CuSe, CuSe and CuS samples.

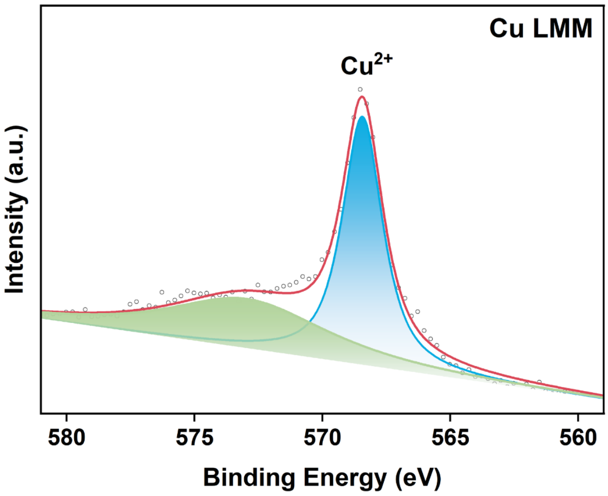

**Fig. S7.** Cu LMM Auger spectra of the CuS@CuSe.

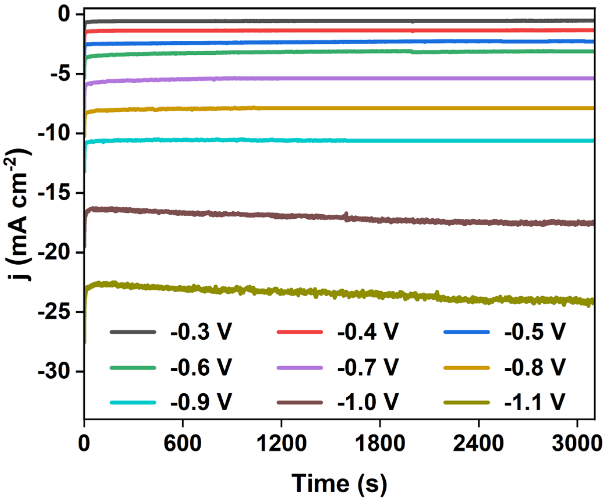

**Fig. S8.** Chronoamperometry curves at various potentials in $CO_2$-saturated 0.5 M $K_2SO_4$ electrolyte.

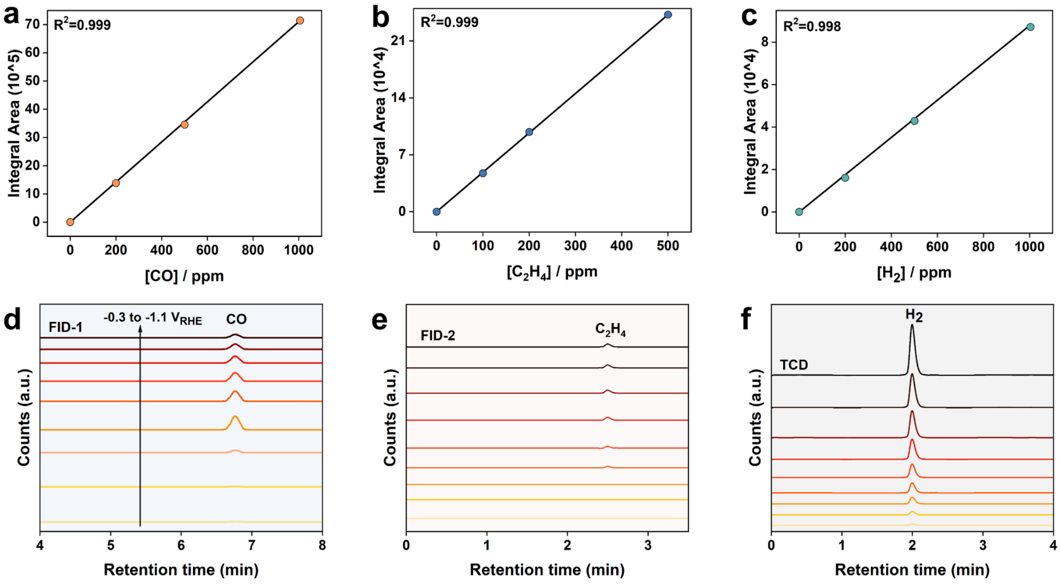

**Fig. S9.** Calibration curves for CO (a), $C_2H_4$ (b) and $H_2$ (c). Based on these calibration curves, the concentration of gas products produced was quantified accurately. Representative GC spectrum of the gas phase products based on the FID detector (d, e) and TCD-detector (f) for the CuS@CuSe heterostructure catalysts during $CO_2$ electroreduction process.

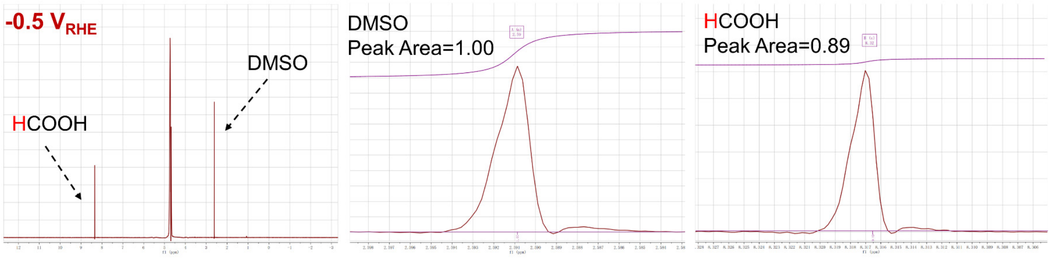

**Fig. S10.** $^1$H NMR spectra of CO$_2$RR products and DMSO internal standard at –0.5 V$_{RHE}$ with integrated peak area indicated.

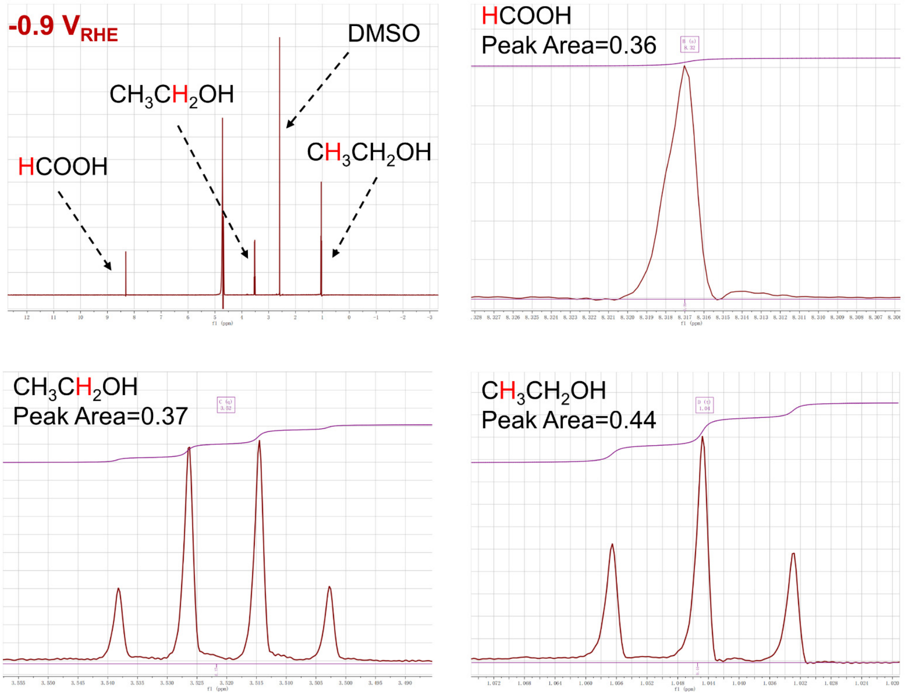

**Fig. S11.** $^1$H NMR spectra of $CO_2$RR products and DMSO internal standard at –0.9 V$_{RHE}$ with integrated peak area indicated.

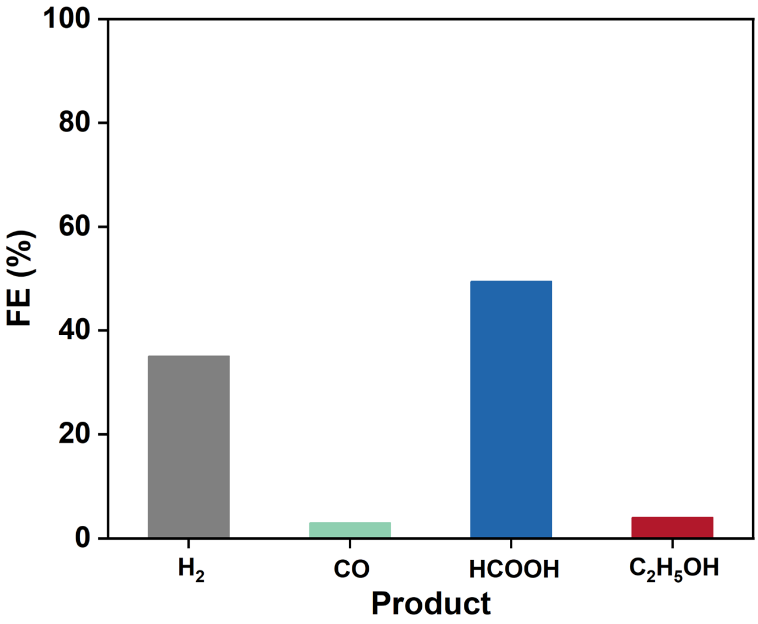

**Fig. S12.** FE of $H_2$, CO, HCOOH and $C_2H_5OH$ for CuS@CuSe-0.9 V at −0.5 $V_{RHE}$.

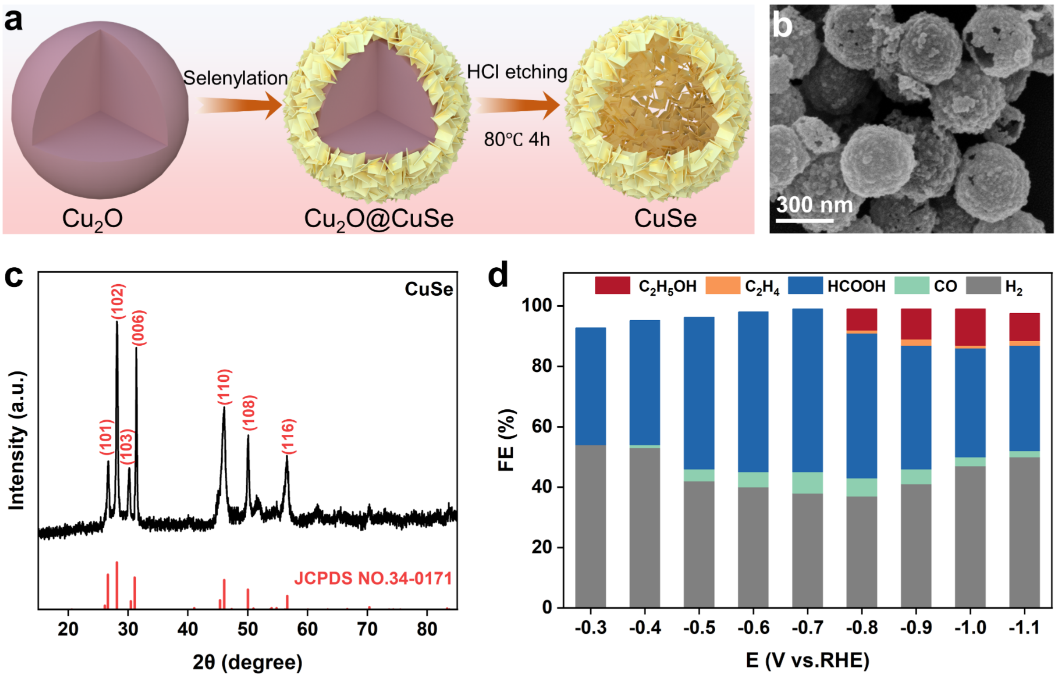

**Fig. S13.** (a) Schematic illustration of the synthesis procedure of CuSe hollow microspheres. Typical SEM image (b) and XRD pattern (c) of the CuSe sample. (d) Product distribution and corresponding FE within the potentials range from −0.3 to −1.1 $V_{RHE}$.

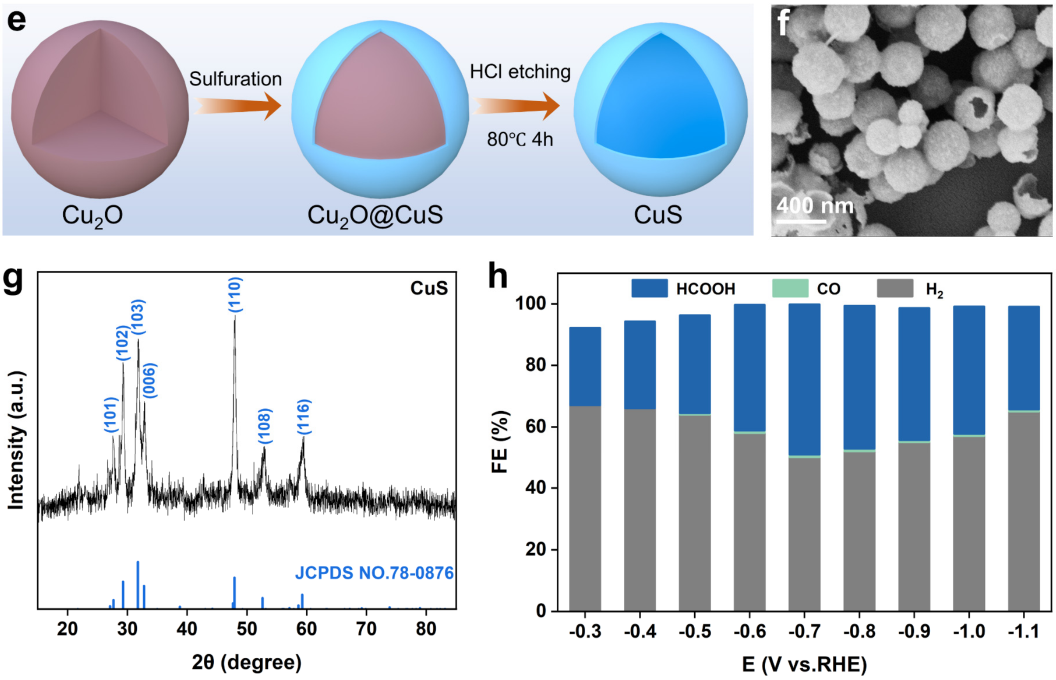

**Fig. S14.** (a) Schematic illustration of the synthesis procedure of CuS hollow microspheres. Typical SEM image (b) and XRD pattern (c) of the CuS sample. (d) Product distribution and corresponding FE within the potentials range from −0.3 to −1.1 VRHE.

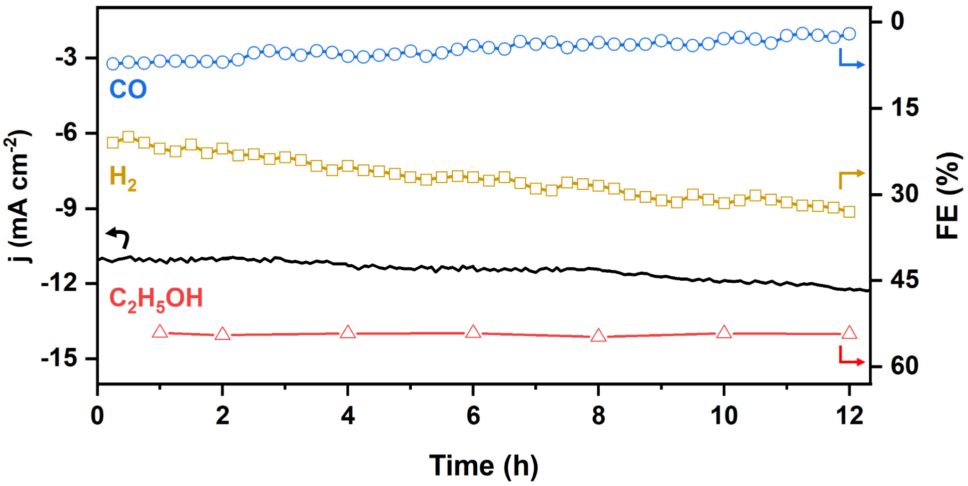

**Fig. S15.** Chronopotentiometry test and the corresponding FEs of CO, $H_2$ and $C_2H_5OH$ at −0.9 $V_{RHE}$ for 12 h. The CO FE shows a gradual decrease due to the dimerization depletion.

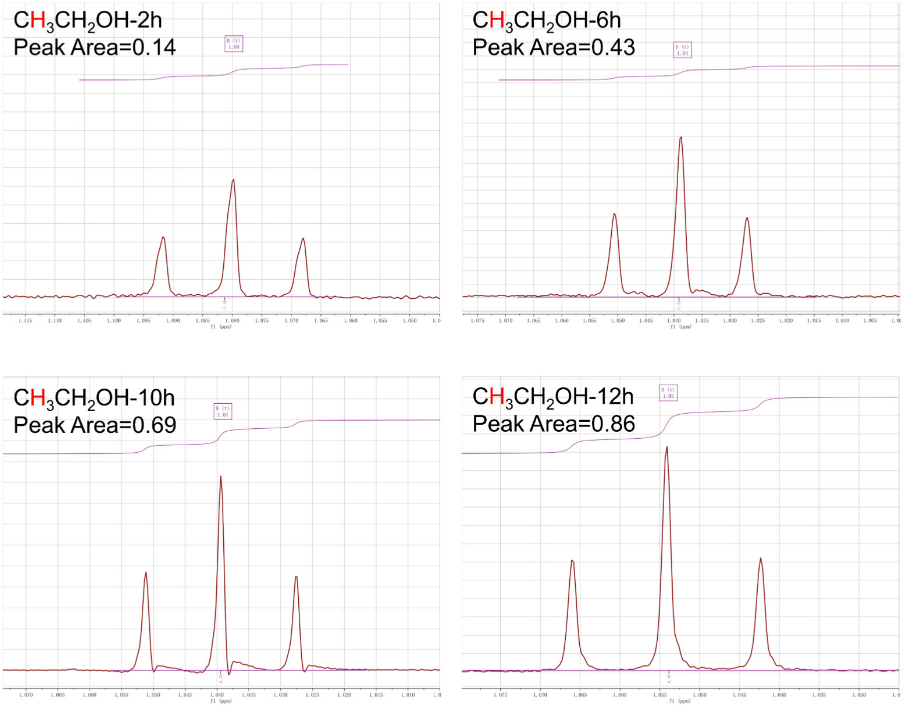

**Fig. S16.** $^1$H NMR spectra of $CH_3CH_2OH$ after $CO_2$RR with different electrolysis times at –0.9 $V_{RHE}$ with integrated peak area.

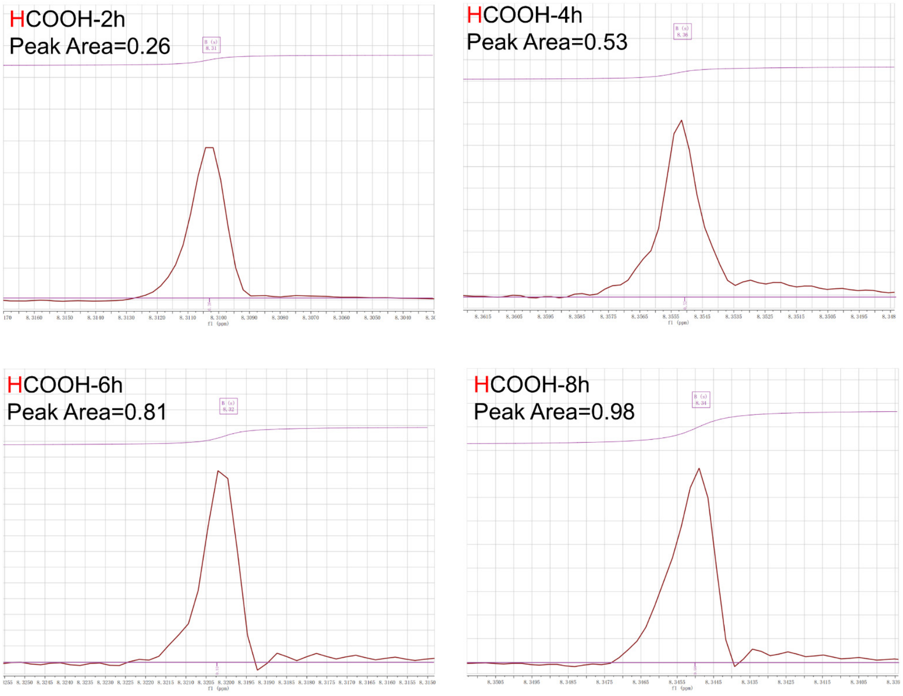

**Fig. S17.** $^1$H NMR spectra of HCOOH after $CO_2$RR with different electrolysis times at –0.5 $V_{RHE}$ with integrated peak area.

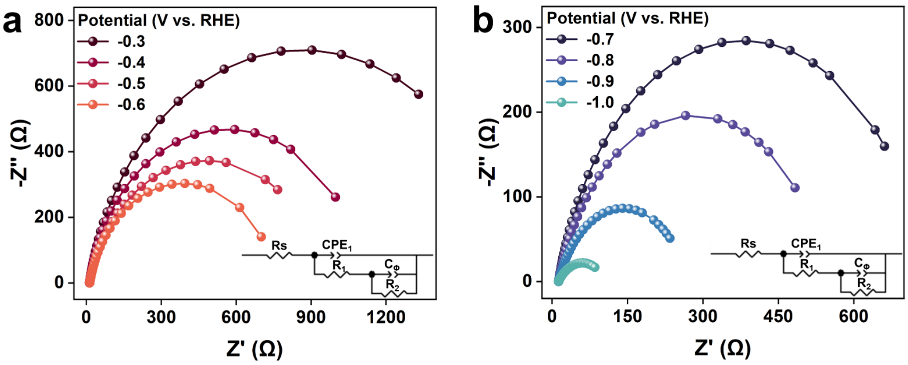

**Fig. S18.** Nyquist plots measured in the (a) low potentials (–0.3 ~ –0.6 V$_{RHE}$) and (b) high potentials (–0.7 ~ –1.0 V$_{RHE}$) interval. The scattered symbol represents the experimental results, and the solid lines represent simulated fitting results. The inset shows the equivalent circuit for the simulation.

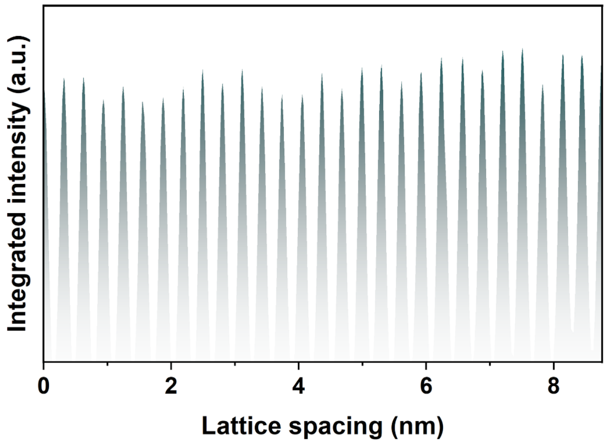

**Fig. S19.** The lattice spacing obtained by integrating a few atomic layers of the pristine CuS@CuSe sample.

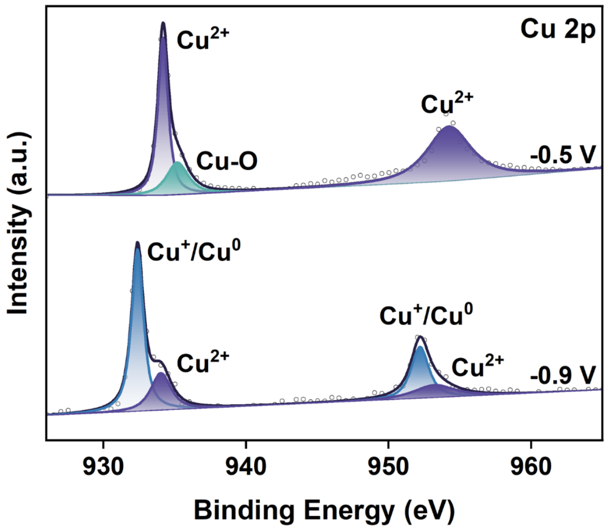

**Fig. S20.** High resolution XPS spectra in Cu 2p region of the catalyst under –0.5 $V_{RHE}$ and –0.9 $V_{RHE}$, respectively.

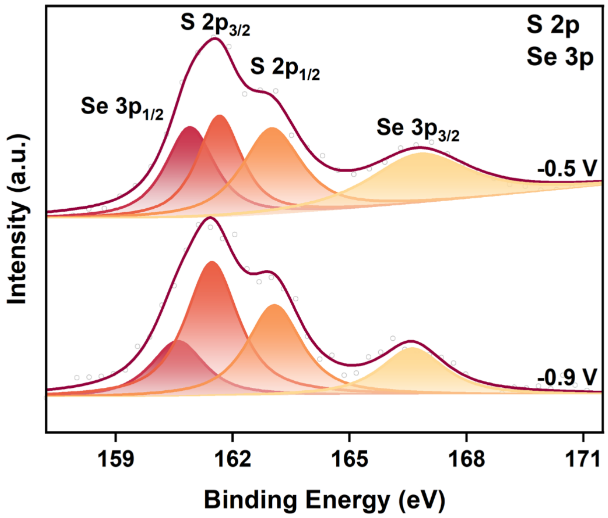

**Fig. S21.** High resolution XPS spectra in S 2p/Se 3p region of the catalyst under –0.5 V$_{RHE}$ and –0.9 V$_{RHE}$, respectively.

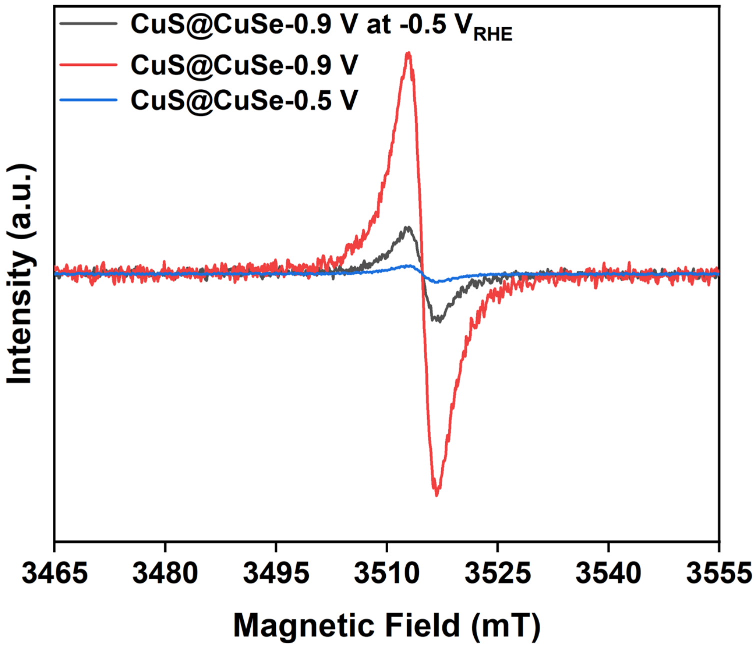

**Fig. S22.** EPR spectra of CuS@CuSe-0.5 V, CuS@CuSe-0.9 V, and CuS@CuSe-0.9 V at −0.5 V$_{RHE}$.

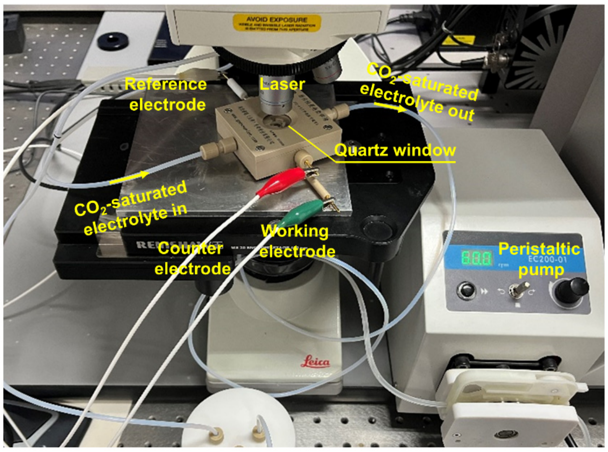

**Fig. S23.** Photograph of the electrochemical *in situ* Raman set-up.

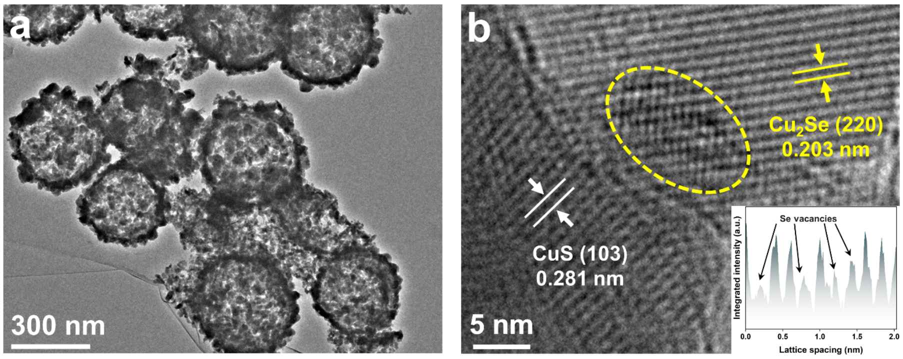

**Fig. S24.** (a) TEM image and (b) HRTEM image of the CuS@$Cu_2Se$-$V_{Se}$ after a 12 hours stability test at –0.9 $V_{RHE}$, the inset corresponds to the lattice spacing.

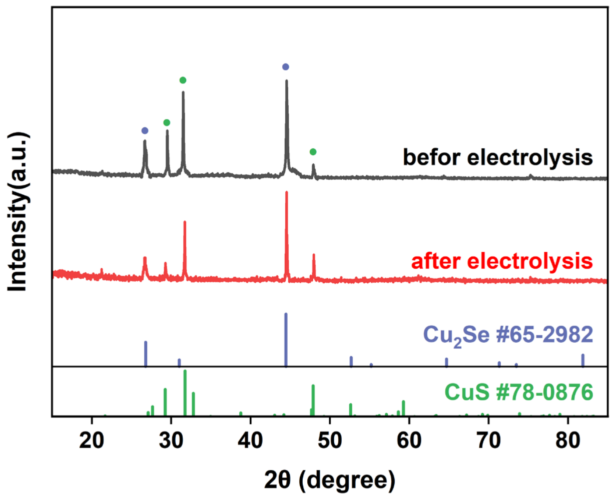

**Fig. S25.** XRD patterns of the CuS@Cu$_2$Se-$V_{Se}$ before and after a 12 hours stability test at −0.9 $V_{RHE}$, respectively.

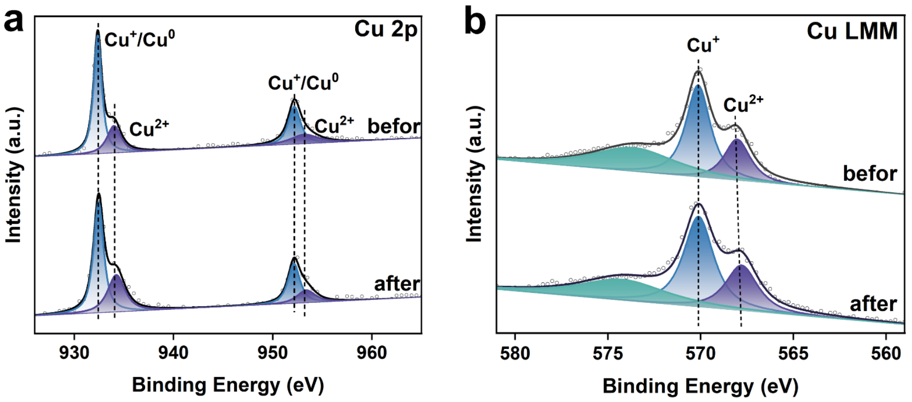

**Fig. S26.** High resolution XPS spectra in Cu 2p region (a) and Cu LMM Auger spectra (b) of the CuS@$Cu_2Se$-$V_{Se}$ before and after a 12 hours stability test at –0.9 $V_{RHE}$, respectively.

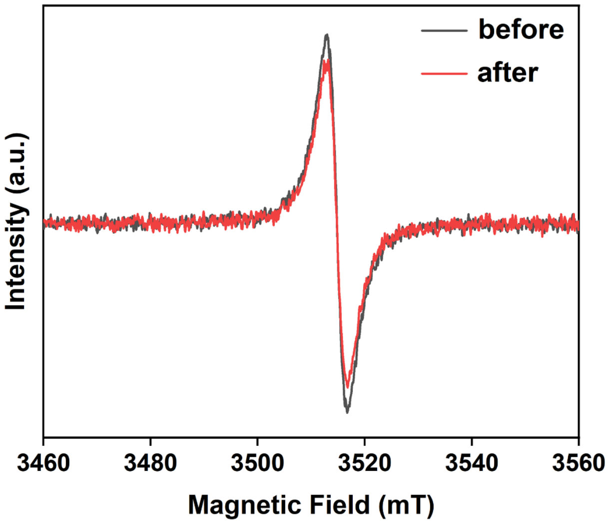

**Fig. S27.** EPR spectras of the CuS@$Cu_2Se$-$V_{Se}$ before and after a 12 hours stability test at –0.9 $V_{RHE}$, respectively.

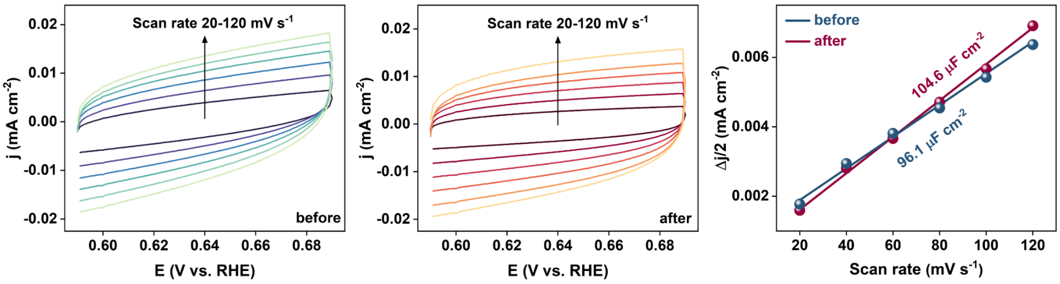

**Fig. S28.** Cyclic voltammograms and the electrochemical double-layer capacitance ($C_{dl}$) of CuS@$Cu_2Se$-$V_{Se}$ before and after a 12 hours stability test at –0.9 $V_{RHE}$.

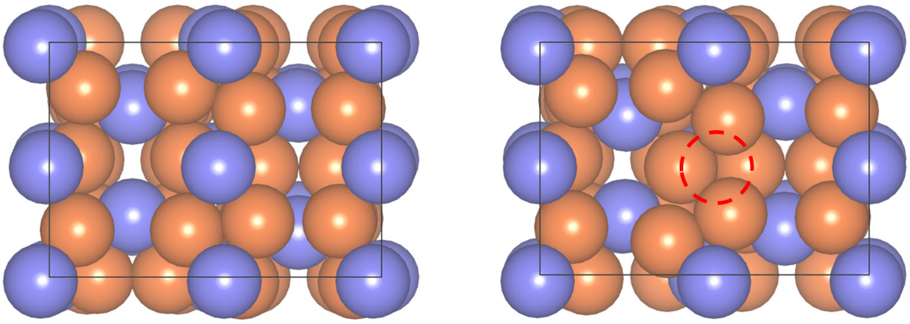

Cu$_2$Se (220)

Cu$_2$Se-$V_{Se}$ (220)

**Fig. S29.** Top view of the optimized atomic configurations of Cu$_2$Se (220) surface without and with one Se vacancy.

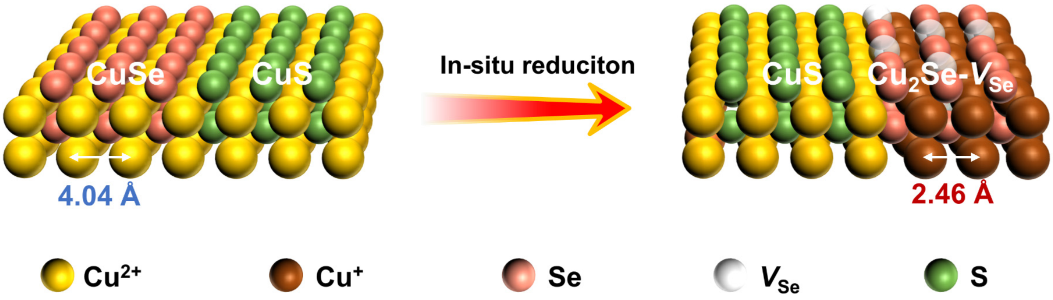

**Fig. S30.** Schematic representation of the reconstitution process from the CuS@CuSe to the CuS@$Cu_2Se$-$V_{Se}$.

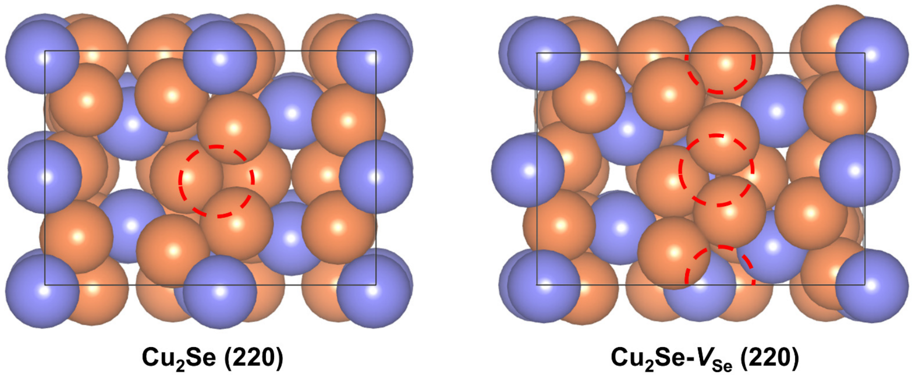

**Fig. S31.** Top view of the optimized atomic configurations of $Cu_2Se$ (220) surface with one Se vacancy and two Se vacancies.

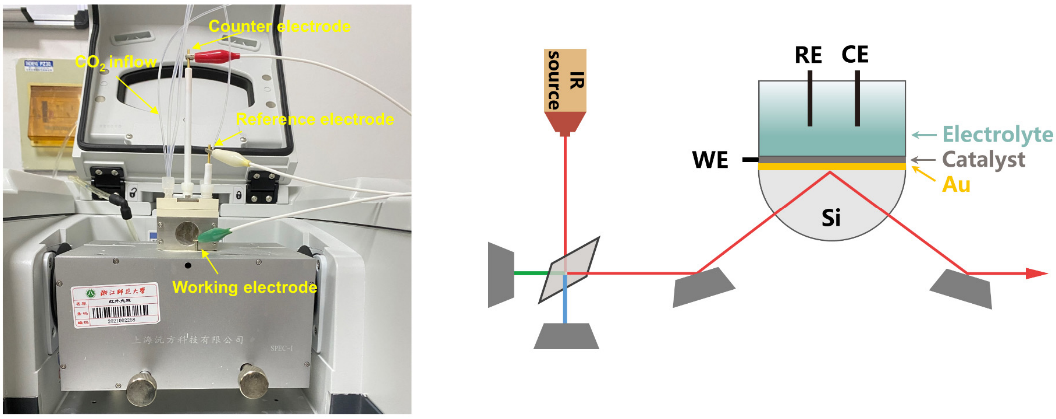

**Fig. S32.** A photograph and schematic illustration of electrochemical ATR-SEIRAS apparatus in this work with catalysts cast on Au/Si prism as working electrode.

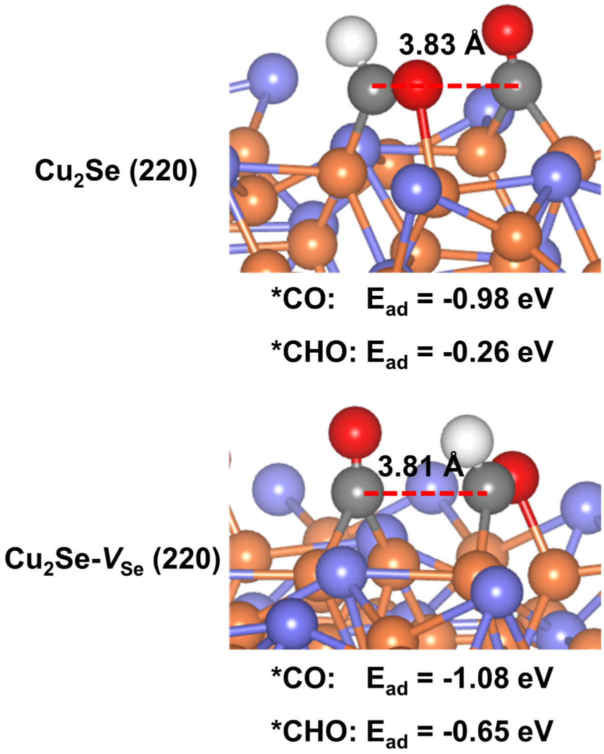

**Fig. S33.** Adsorption energies of *CO and *CHO in the (*CO+*CHO) co-adsorption mode on $Cu_2Se$ (220) and $Cu_2Se$-$V_{Se}$ (220) surface.

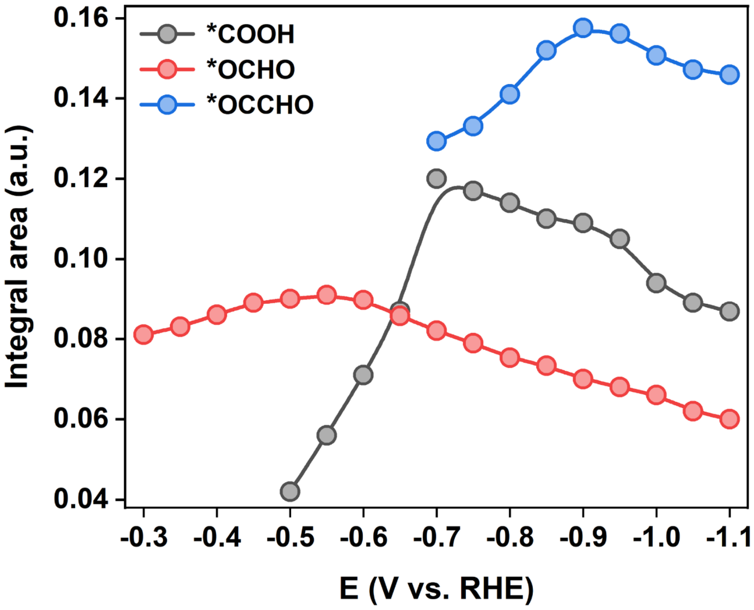

**Fig. S34.** The potential-dependent *COOH, *OCHO and *OCCHO peak-integrated intensities collected in 0.5 M $K_2SO_4$ solution saturated with $^{12}CO_2$.

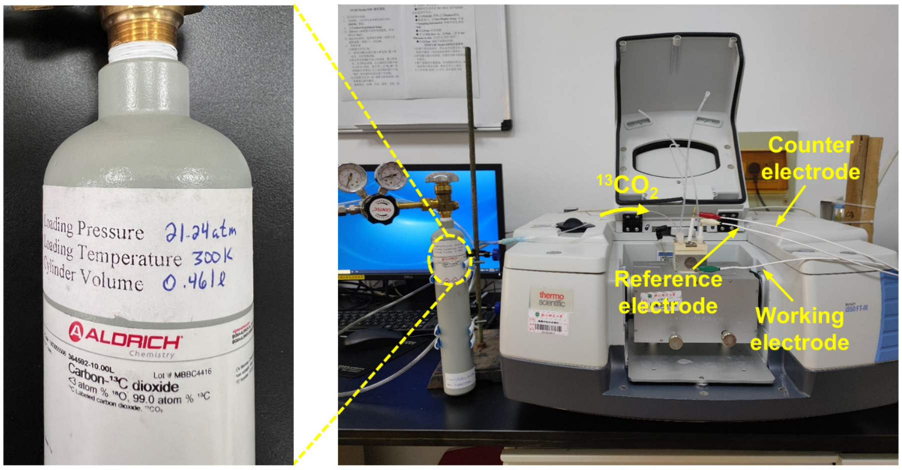

**Fig. S35.** A photograph of electrochemical ATR-SEIRAS apparatus with a $^{13}CO_2$ isotope labelling.

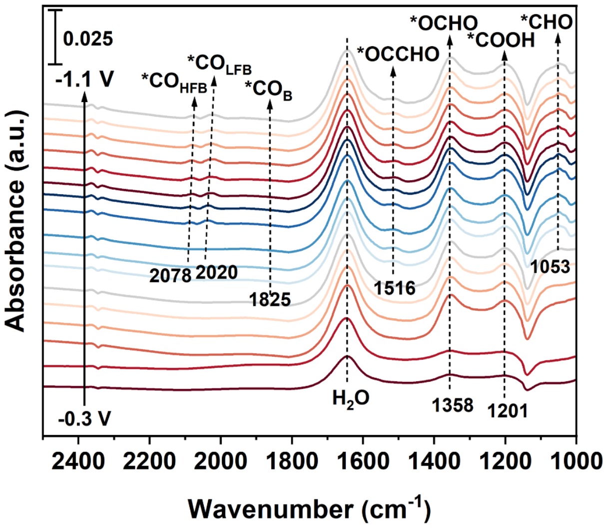

**Fig. S36.** Potentiodynamic *in situ* ATR-SEIRA spectra of the CuS@CuSe catalysts feeding with $^{13}CO_2$ in 0.5 M $K_2SO_4$ aqueous solution, a single-beam spectrum taken at 0.0 $V_{RHE}$ as the reference.

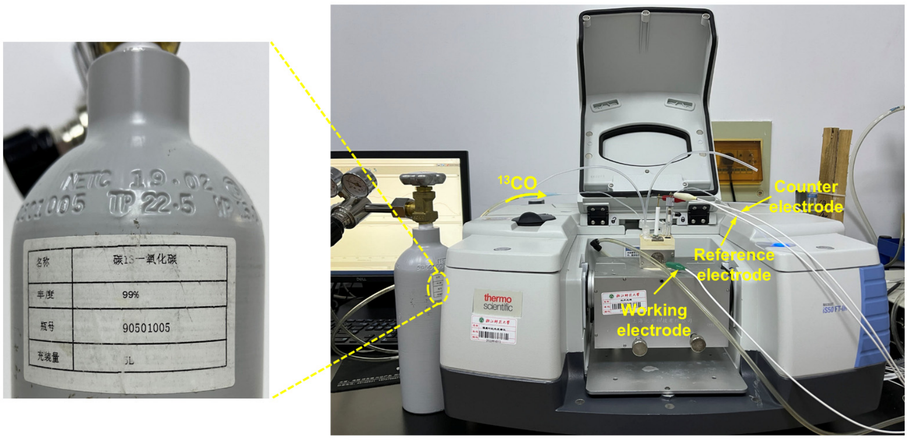

**Fig. S37.** A photograph of electrochemical ATR-SEIRAS apparatus with a $^{13}$CO isotope labelling.

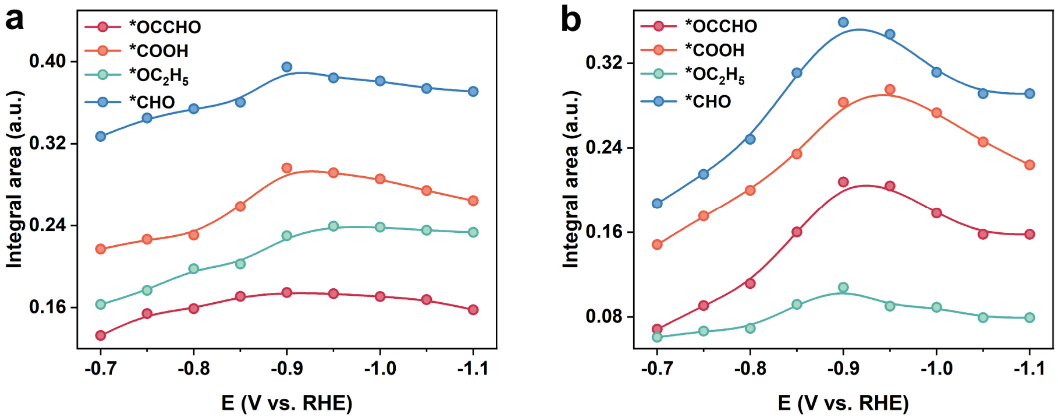

**Fig. S38.** The potential-dependent *OCCHO, *COOH, *$OC_2H_5$ and *CHO peak-integrated intensities collected in 0.5 M $K_2SO_4$ solution saturated with $^{12}$CO (a) and $^{13}$CO (b).

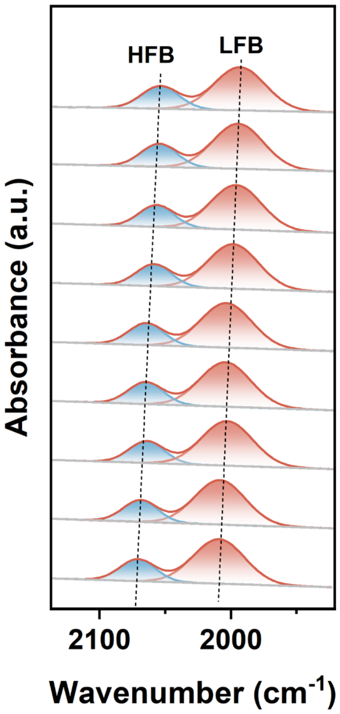

**Fig. S39.** Potentiodynamic ATR-SEIRA spectra of the $*CO_L$ regions in $^{13}CO$ atmosphere.

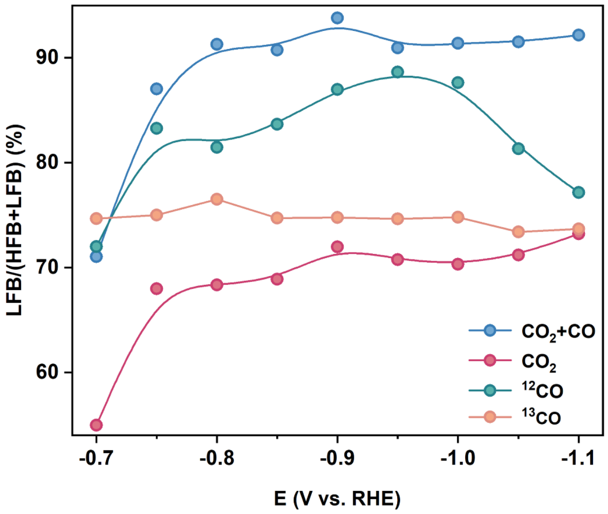

**Fig. S40.** Comparison of the LFB/(HFB+LFB) ratio as a function of applied potential.

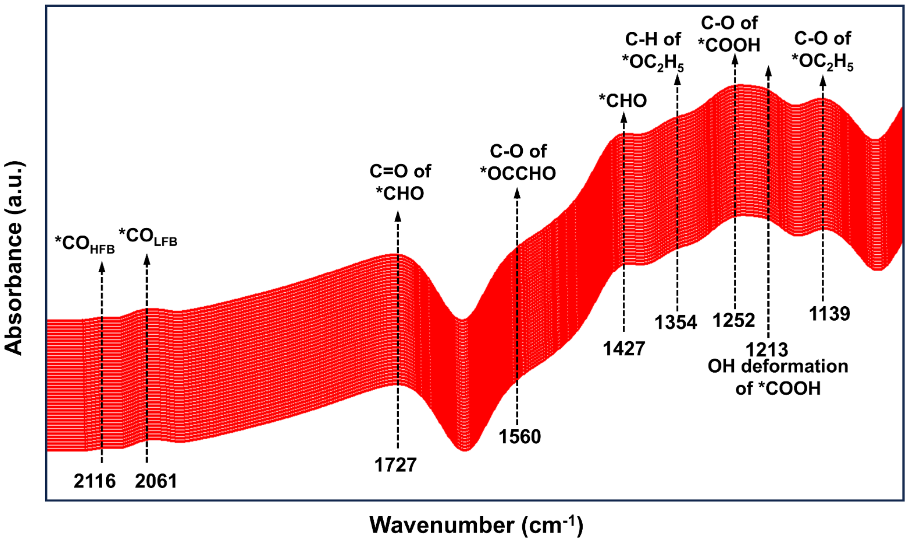

**Fig. S41.** Time-evolved ATR-SEIRA spectra during $CO_2$ electrolysis at −0.9 $V_{RHE}$.

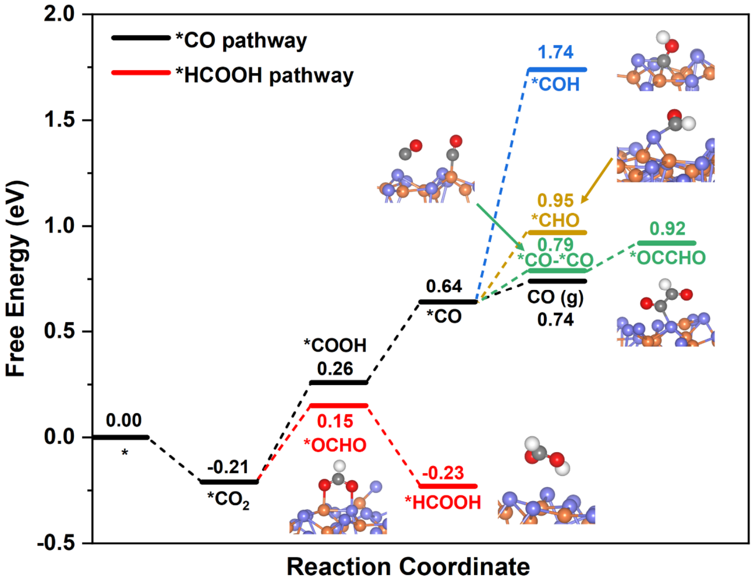

**Fig. S42.** The free energies of the HCOOH pathway and CO pathway (including the *CO desorption, hydrogenation and dimerization) for CuSe (110). The insets show adsorption model plots of *OCHO, *COH, *CHO, *CO-*CO and *OCCHO intermediates.

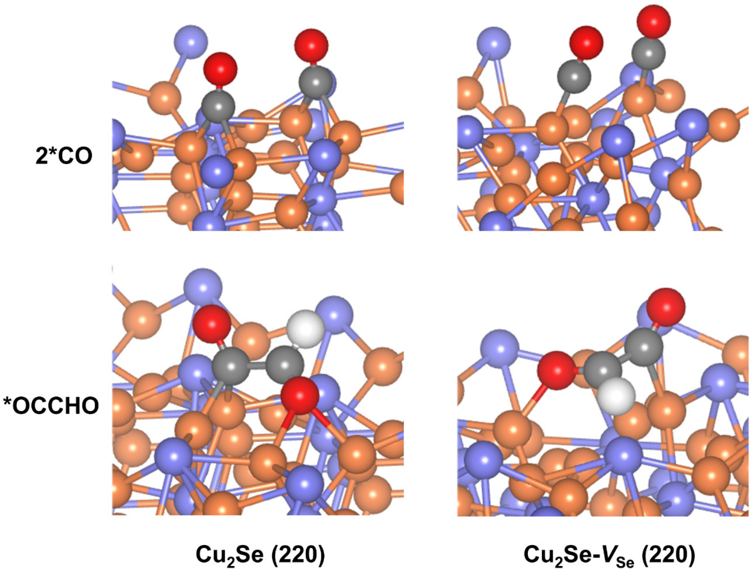

**Fig. S43.** Adsorption model plots of the 2*CO, *OCCHO on $Cu_2Se$ (220) and $Cu_2Se$-$V_{Se}$ (220), respectively.

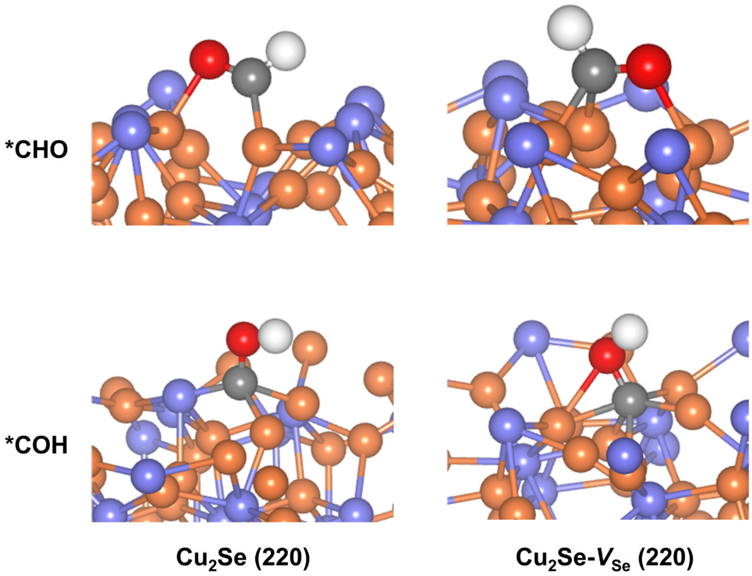

**Fig. S44.** Adsorption model plots of the *CHO and *COH on $Cu_2Se$ (220) and $Cu_2Se$-$V_{Se}$ (220), respectively.

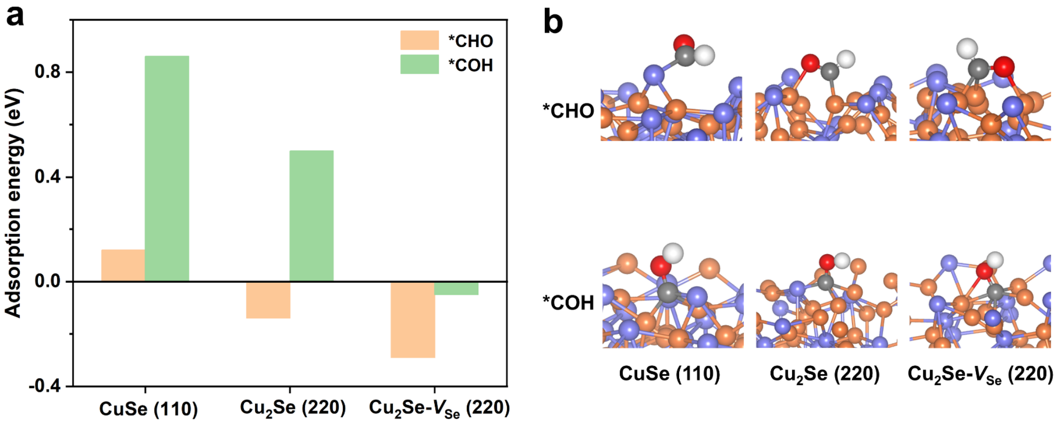

**Fig. S45.** The adsorption energy (a) and corresponding adsorption model (b) of *CHO and *COH on the catalyst surface of CuSe (110), $Cu_2Se$ (220) and $Cu_2Se$-$V_{Se}$ (220). The white, gray, red, purple, and orange spheres represent H, C, O, Se, and Cu atoms, respectively.

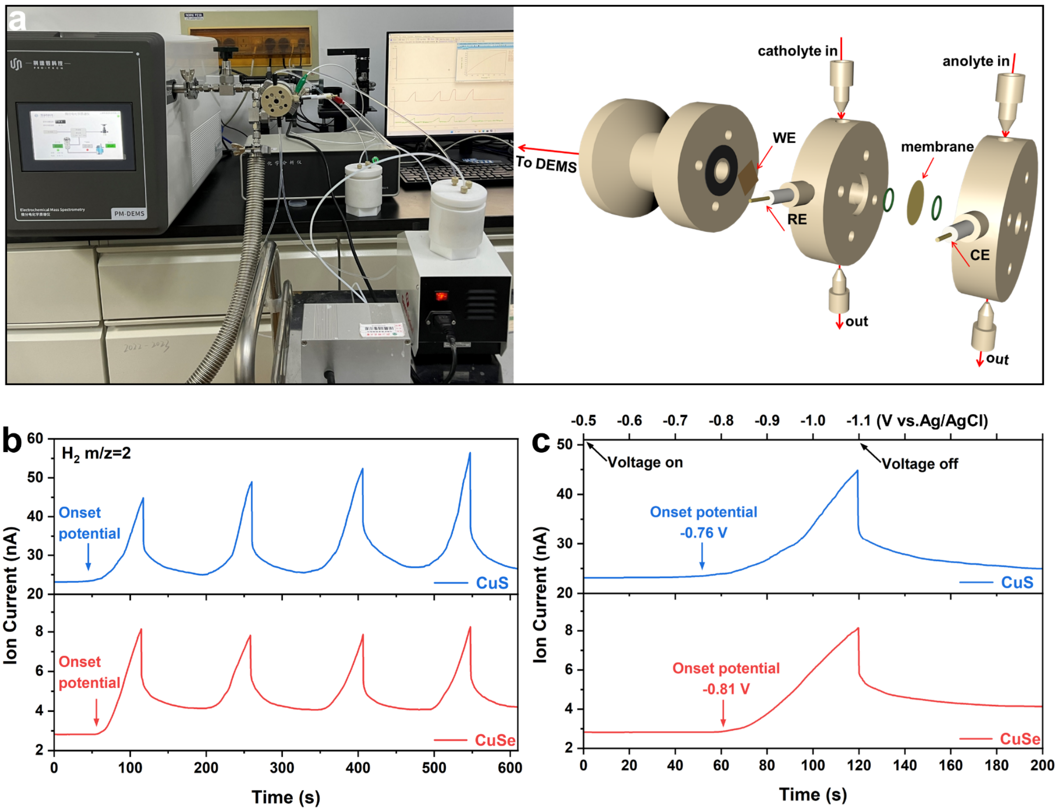

**Fig. S46** (a) Photograph of in-situ DEMS setup and 3D explosion view of the customized DEMS flow cell. In-situ DEMS results (b) and local magnification (c) of the $H_2$ evolution during the electrochemical $CO_2RR$ in $CO_2$-saturated 0.5 M $K_2SO_4$ aqueous solution on CuS and CuSe, respectively.

**Table S1.** The fitted parameters of the EIS data under different applied potentials.

| **Potential (V vs. RHE)** | **Rs (Ω)** | **$CPE_1$ ($F_s^{n-1}$)** | **$R_1$ (Ω)** | **$R_2$ (Ω)** | **$C_φ$ (F)** |
|---|---|---|---|---|---|
| −0.3 | 11.23 | 0.7216 | 17.05 | 1040.5 | 1.013 |
| −0.4 | 11.27 | 0.7771 | 12.87 | 874.1 | 1.027 |
| −0.5 | 11.73 | 0.7580 | 13.28 | 694.5 | 1.031 |
| −0.6 | 11.61 | 0.7349 | 14.08 | 481.0 | 1.023 |
| −0.7 | 11.72 | 0.7583 | 12.72 | 520.2 | 0.9081 |
| −0.8 | 11.84 | 0.6287 | 8.934 | 282.2 | 0.9217 |
| −0.9 | 11.57 | 0.7105 | 12.12 | 157.5 | 0.9667 |
| −1.0 | 11.42 | 0.6199 | 11.75 | 86.1 | 0.9206 |

**Table S2.** Comparison of IR shifts in 0.5 M $K_2SO_4$ solutions saturated with $^{12}CO_2$ and $^{13}CO_2$ atmosphere, respectively.

| **Feeding gas** | **Wavenumber (cm$^{-1}$)** | | | | | | |
|---|---|---|---|---|---|---|---|
| | *CO$_{HFB}$ | *CO$_{LFB}$ | *CO$_B$ | C−O of *OCCHO | *v*(C−O) of *OCHO | C−O of *COOH | *v*(O=C−H) of *CHO |
| $^{12}CO_2$ | 2126 | 2065 | 1855 | 1563 | 1400 | 1247 | 1090 |
| $^{13}CO_2$ | 2078 | 2020 | 1825 | 1516 | 1358 | 1201 | 1053 |

**Table S3.** Comparison of IR shifts in 0.5 M $K_2SO_4$ solutions saturated with $^{12}CO$ and $^{13}CO$ atmosphere, respectively.

| **Feeding gas** | **Wavenumber (cm$^{-1}$)** | | | | | | | | |
|---|---|---|---|---|---|---|---|---|---|
| | $^{*}CO_{HFB}$ | $^{*}CO_{LFB}$ | C=O of *CHO | C−O of *OCCHO | *CHO | C−H of $^{*}OC_2H_5$ | C−O of *COOH | OH of *COOH | C−O of $^{*}OC_2H_5$ |
| $^{12}CO$ | 2116 | 2061 | 1727 | 1560 | 1427 | 1354 | 1252 | 1213 | 1139 |
| $^{13}CO$ | 2071 | 2007 | 1693 | 1512 | 1378 | 1309 | 1213 | 1163 | 1088 |

## Rerference

1. Yan, Q.-X. Li, S.-J. Huo, M. Ma, W.-B. Cai and M. Osawa, Ubiquitous Strategy for Probing ATR Surface-Enhanced Infrared Absorption at Platinum Group Metal−Electrolyte Interfaces, *J. Phys. Chem. B*, 2005, **109**, 7900-7906.
2. G. Kresse and J. Furthmüller, Efficiency of ab-initio total energy calculations for metals and semiconductors using a plane-wave basis set, *Comput. Mater. Sci.*, 1996, **6**, 15-50.
3. G. Kresse and J. Furthmüller, Efficient iterative schemes for ab initio total-energy calculations using a plane-wave basis set, *Phys. Rev. B*, 1996, **54**, 11169-11186.
4. J. P. Perdew, K. Burke and M. Ernzerhof, Generalized Gradient Approximation Made Simple, *Phys. Rev. Lett.*, 1996, **77**, 3865-3868.
5. S. Grimme, J. Antony, S. Ehrlich and H. Krieg, A consistent and accurate ab initio parametrization of density functional dispersion correction (DFT-D) for the 94 elements H-Pu, *J. Chem. Phys.*, 2010, **132**, 154104.
6. G. Kresse and D. Joubert, From ultrasoft pseudopotentials to the projector augmented-wave method, *Phys. Rev. B*, 1999, **59**, 1758-1775.
7. P. E. Blöchl, Projector augmented-wave method, *Phys. Rev. B*, 1994, **50**, 17953-17979.
8. H. J. Monkhorst and J. D. Pack, Special points for Brillouin-zone integrations, *Phys. Rev. B*, 1976, **13**, 5188-5192.
9. V. I. Anisimov, J. Zaanen and O. K. Andersen, Band theory and Mott insulators: Hubbard U instead of Stoner I, *Phys. Rev. B*, 1991, **44**, 943-954.
10. S. Kumari, A. N. Alexandrova and P. Sautet, Nature of Zirconia on a Copper Inverse Catalyst Under CO2 Hydrogenation Conditions, *J. Am. Chem. Soc.*, 2023, **145**, 26350-26362.
11. J. K. Nørskov, J. Rossmeisl, A. Logadottir, L. Lindqvist, J. R. Kitchin, T. Bligaard and H. Jónsson, Origin of the Overpotential for Oxygen Reduction at a Fuel-Cell Cathode, *J. Phys. Chem. B*, 2004, **108**, 17886-17892.
12. H. Wang, X. Bi, Y. Yan, Y. Zhao, Z. Yang, H. Ning and M. Wu, Efficient Electrocatalytic Reduction of $CO_2$ to Ethanol Enhanced by Spacing Effect of Cu-Cu in $Cu_{2-x}Se$ Nanosheets, *Adv. Funct. Mater.*, 2023, **33**, 2214946.
13. W. Sun, P. Wang, Y. Jiang, Z. Jiang, R. Long, Z. Chen, P. Song, T. Sheng, Z. Wu and Y. Xiong, V-Doped $Cu_2Se$ Hierarchical Nanotubes Enabling Flow-Cell $CO_2$ Electroreduction to Ethanol with High Efficiency and Selectivity, *Adv. Mater.*, 2022, **34**, 2207691.
14. V. Wang, N. Xu, J.-C. Liu, G. Tang and W.-T. Geng, VASPKIT: A user-friendly interface facilitating high-throughput computing and analysis using VASP code, *Comput. Phys. Commun.*, 2021, **267**, 108033.
15. K. Momma and F. Izumi, VESTA 3 for three-dimensional visualization of crystal, volumetric and morphology data, *J. Appl. Crystallogr.*, 2011, **44**, 1272-1276.